Dendrite -Free Potassium Metal Anodes in a Carbonate Electrolyte

Pengcheng Liu,[1] Yixian Wang,[1] Qilin Gu,[2] Jagjit Nanda [3], John Watt,[4] David Mitlin [1]

[1] Walker Department of Mechanical Engineering, The University of Texas at Austin, Austin, TX, 78712-1591, USA

[2] Department of Materials Science and Engineering, Faculty of Engineering, National University of Singapore, Singapore 117574, Singapore

[3] Chemical Sciences Division, Oak Ridge National Laboratory, Oak Ridge, TN USA,

[4] Center for Integrated Nanotechnologies, Los Alamos National Laboratory, Los Alamos, NM 87545, USA

keywords: potassium ion battery (KIB, PIB); potassium sulfur battery; lithium metal anode; sodium metal anode; solid electrolyte interphase (SEI).

Potassium (K) metal anodes suffer from a challenging problem of dendrite growth. Here we demonstrate that a tailored current collector will stabilize the metal plating-stripping behavior even with a conventional KPF_6-carbonate electrolyte. A three-dimensional copper current collector was functionalized with partially reduced graphene oxide to create a potassiophilic surface, the electrode being denoted as rGO@3D-Cu. Potassiophilic *vs.* potassiophobic experiments demonstrate that molten K fully wets rGO@3D-Cu after 6 seconds, but does not wet unfunctionalized 3D-Cu. Electrochemically, a unique synergy is achieved that is driven by interfacial tension and geometry: The adherent rGO underlayer promotes two-dimensional layer-by-layer (Frank–van-der-Merwe) metal film growth at early stages of plating, while the tortuous 3D-Cu electrode reduces the current density and geometrically frustrates dendrites. The rGO@3D-Cu symmetric cells and half-cells achieve state-of-the-art plating and stripping performance. The symmetric rGO@3D-Cu cells exhibit stable cycling at 0.1 - 2 mA cm^{-2}, while baseline Cu prematurely failed when the current reached 0.5 mA cm^{-2}. The half-cells cells of rGO@3D-Cu (no K reservoir) are stable at 0.5 mA cm^{-2} for 10,000 minutes (100 cycles), and at 1 mA cm^{-2} for 5,000 minutes. The baseline 3D-Cu, planar rGO@Cu and planar Cu foil failed after 5,110, 3,012 and 1,410 minutes, respectively.

With the rapid development of large-scale energy storage systems, "Beyond LIB" battery chemistries are attracting extensive attention, including metal batteries (MBs) based on a high-energy low-voltage alkaline metal anodes.[1, 2, 3, 4, 5] While numerous publications often cite an impending "Li Shortage" as the motivation for Beyond LIB studies, the situation is not that dire. In fact, a recent in-depth techno-economic study concluded that a potential Li scarcity *per se* is not a credible threat to wider commercialization of electric vehicles.[6] Prior Li precursor shortages that were manifested as price spikes were caused by poor planning practices, which did not properly anticipate the short-term increases in demand. The natural lithium carbonate precursors were available but could not be processed and delivered to the market in a timely manner. The motivation for potassium and sodium batteries may then be viewed as the potential to deliver a complementary technology to LIBs to the general consumers. For example, stationary energy storage and grid-level energy storage are already diversified to include aqueous technologies and would benefit from additional low-cost options.

In principle, potassium also possesses some electrochemical advantages.[1, 7] It has a weaker Lewis acidity than Li and Na, resulting in a smaller Stokes' radius (3.6 Å vs. 4.8 Å and 4.6 Å) in carbonate solvents.[8, 9] In a carbonate electrolyte, K^+ obtains the highest ion mobility, ion conductivity and ion transport number of the three ions.[8, 9] Moreover, in organic electrolytes K has a lower redox voltage than Li and Na (-0.09 V vs. 0 V and 0.23 V), implying that in principle a high voltage for a full battery may be possible.[8, 10] Moreover, the achievable energy difference between potassium and sodium ion batteries is not as large as is often perceived. A recent study that analyzed existing commercial cell architectures concluded that sodium and potassium batteries are capable of achieving 83% and 78% the energy of lithium batteries, respectively.[11] Though far behind lithium and sodium metal batteries in terms of their development,[4, 12, 13] potassium metal batteries (KMBs, PMBs) are beginning to attract attention.[14-22] The potassium metal gives a specific capacity (687 mAh g^{-1}), which is almost twice that of graphite with lithium, and generally far surpassing that of most KIB anodes. Obtaining stable potassium plating and stripping is crucial, and failure to achieve this can ruin the performance of any optimized KMB cathode architecture. There have been extensive research to understand lithium metal anodes in terms of basic phenomenology of the plating/stripping process, the role of electrolytes and electrode architectures in SEI formation, the origin and control of dendrite growth, *etc.*[3, 5, 13, 23] To date there are far fewer fundamental studies on potassium metal anodes, an area that is promising for further exploration.

Realizing a stable K metal anode remains challenging due to the inherent higher reactivity of K metal as compared to Li, which leads to unstable solid electrolyte interphase (SEI) and the ultimate growth of dendrites.[5, 14, 17] There have been several notable successes for stable plating/stripping of K metal, which were based on clever electrolyte design. Authors found that high-concentrated potassium bis(fluoroslufonyl)imide (KFSI)- dimethoxyethane (DME) electrolyte forms a uniform SEI on the surface of potassium, enabling reversible plating/stripping electrochemistry at ambient temperature.[14, 16, 24] By comparison, electrolytes of 1 M potassium hexafluorophosphate (KPF_6)-DME, 1 M KTFSI-DME, and 0.8 M KPF_6 in EC/DEC all led to cell failure within 10−20 cycles.[14] The super-concentrated KFSI-DME electrolyte (mole ratio = 0.1 of KFSI/DME = 0.1 and 0.5) can efficiently passivate the K surface and enable reversible K plating and stripping electrochemistry with a high CE (~99%) and relatively long life (100 cycles).[14] In another study, the authors applied an electrochemical polishing method to create ultra-smooth ultra-thin solid-electrolyte interphase layers resulting in stable Li, Na, K anodes in FSI-DME electrolytes.[18] Researchers cleverly employed a puffed millet/NiO slurry[17] or K melt-infiltrated carbon nanotube membranes[19] to stabilize the metal front. Goodenough *et al.* employed a deep eutectic Na−K alloy to promote self-healing through the formation of a liquid phase.[21] It was also found that liquid Na–K alloy coated by thin solid K_2O layer exhibits a self-healing characteristics.[22] Goodenough and Yu also created organic (sodium rhodizonate dibasic, SR)-based Na-K battery that worked well with either charge carrier.[20]

When employing more common and low-cost electrolytes, achieving stable K plating/striping remains a challenge. For example, while its Li analogue is well-established,[25] there have been only two recent reports of the success of K cells with carbonate-based systems.[17, 19] Instead, stable K plating/stripping behavior in most other studies is achieved with KFSI-DME electrolytes. In this study, by tuning the surface energy and the architecture of a copper current collector, we demonstrate stable K plating in a carbonate electrolyte. Symmetric and half-cell metal anodes achieved stable intermediate and high rate cycling in a solution of 0.8 M KPF_6 in ethylene carbonate, diethyl carbonate, propylene carbonate without any additives. Detailed electroanalytical studies combined with thermal wetting infiltration experiments highlight the synergistic and necessary roles of the chemical and the geometrical effects in accomplishing this milestone.

Schematic 1 provides an illustration of the combined self-assembly and partial reduction strategy. The baseline uncoated (as-received) 3D-Cu is also shown on the bottom right. To fabricate rGO@3D-Cu a combined reduction and assembly method was employed. The precursor graphene oxide GO is charged negatively and will be partially reduced by the Cu which will form CuO. Meanwhile metal ions are released, which alter the steady microenvironment of GO and trigger the layer-by-layer stacking of the resultant rGO sheets.[26, 27] It may be observed that with the rGO coating the 3D-Cu foam changes color, with the baseline uncoated 3D-Cu being shown on the bottom right of the schematic. Per the photograph in **Fig. S1**, an 8 cm x 12 cm sheet of rGO@3D-Cu is fabricated in one batch, with larger sheet dimensions being possible by larger reaction vessels.

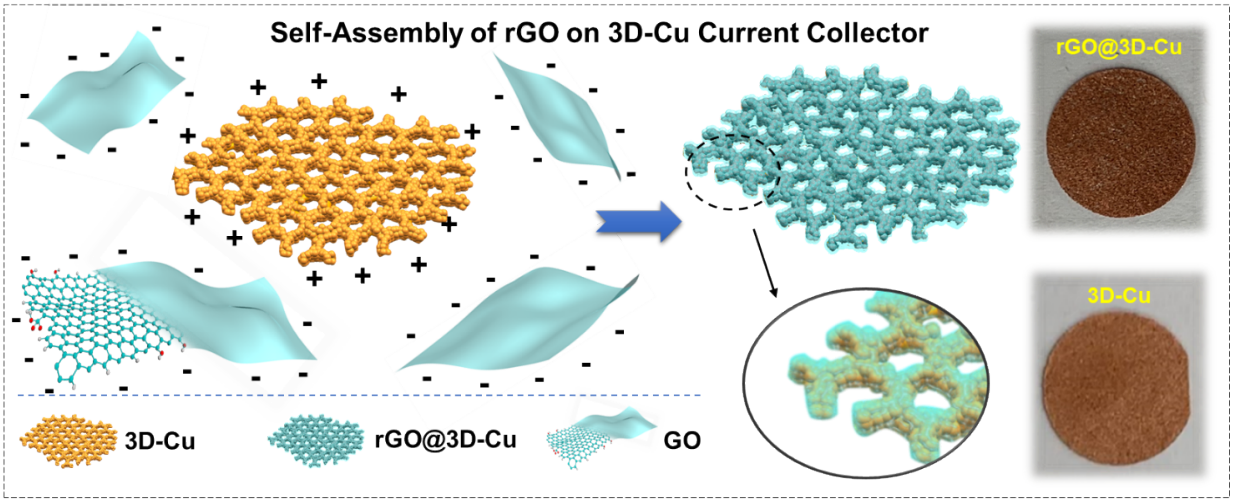

Schematic 1. Fabrication of partially reduced graphene oxide (rGO) coated on a 3D-Cu current collector, termed rGO@3D-Cu. The baseline uncoated (as-received) 3D-Cu is also shown on bottom right.

Figure S2 shows SEM analysis highlighting the pore structure and morphology of the as-received 3D-Cu foil. **Figure 1** primarily highlights the morphology and the surface chemistry of rGO@3D-Cu. As **Figs. 1(a) - 1(c)** indicate, the rGO coating is quite uniform on the 3D-Cu surface, coating the high aspect ratio edges of the foam. The layer appears highly adherent, which is expected from the reactive nature of the GO - Cu interface that leads to rGO. Per the high-resolution SEM images, the thickness of the rGO coating can be estimated to be in the several nanometers in range. The surface of the baseline 3D-Cu is shown in **Fig. 1(d)**, displaying a fairly standard surface topography of a partially sintered compact, with some particulates which were

not removed by the cleaning process. As shown in **Figs. S3(a)** and **S3(b)**, the surface of 3D-Cu shows no Raman or FTIR sensitive signals. **Figures S4(a)** and **S4(b)** show the SEM EDXS analysis of the elemental distribution on the as-received 3D-Cu and rGO@3D-Cu surfaces, respectively. It may be observed that the rGO@3D-Cu is heavily covered by oxygen and carbon, whereas the baseline is not. This is consistent with the X-ray photoelectron spectroscopy (XPS) result of 3D-Cu, shown in **Fig. S5.**

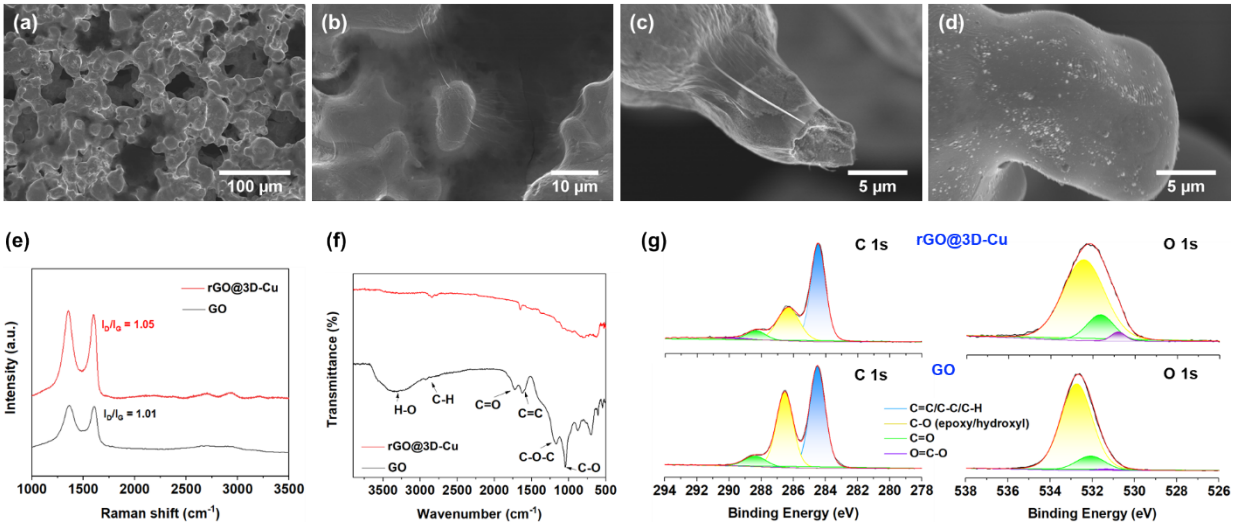

Figure 1. Analytical characterization results for rGO@3D-Cu. **(a) – (c)** SEM images of the rGO@3D-Cu surface, taken at increasing magnifications. **(d)** SEM image the baseline 3D-Cu. **(e)** Raman spectra of the graphene on the rGO@3D-Cu surface, and of the precursor GO. **(f)** FTIR spectra of the graphene on the rGO@3D-Cu surface and precursor GO. **(g)** XPS spectra of core level C 1s and O 1s for the graphene on the rGO@3D-Cu surface and precursor GO.

The electrochemical reaction between the rGO and the Cu surface may be quantitatively analyzed by XPS analysis, Raman spectroscopy analysis and FTIR analysis.[28, 29, 30] **Figure S6** shows the XPS spectra of Cu for as-synthesized rGO@3D-Cu, including the Cu 2p survey spectra, the Cu 2p3/2 fitting profile, and an atomic content table derived from the XPS data. It may be observed that at the XPS profile depth (~ 6 nm) 74at.% of the copper is present as oxidized Cu^{2+}, with remaining 26at.% present in its metallic state. This directly supports the proposed reaction scheme, with strong bonding between the partially reduced rGO and the oxidized copper surface. The Raman analysis shown in **Fig. 1(e)** illustrates only a minor increase in the integrated intensity ratio of the G to D bands, going from 1.01 in GO to 1.05 in rGO. This can be associated with some

elimination of structural and chemical defects,[26, 31] although it is not expected that the partial reduction would change the internal structure of the rGO. **Figure 1(f)** shows the FTIR spectra, which more clearly demonstrates the partial reduction of rGO. For the GO precursor, it is found that the peaks at 1044, 1171, 1734, and 3357 cm^{-1} correspond to the oxygen group of C-O stretching vibrations, C-O-C stretching vibrations, C=O stretching vibrations, and O-H stretching vibrations, respectively.[28, 32] Furthermore, the peaks at 1631 and 2912 cm^{-1} correspond to C=C skeletal vibrations and C-H stretching. In comparison, for rGO@3D-Cu, the peak intensity of oxygen-containing groups is weaker, while the O-H peak almost disappears.

XPS analysis gives further quantitative evidence for partial reduction of rGO on 3D-Cu. The XPS results for rGO@3D-Cu and GO precursor are shown in **Figs. 1(g)**, **S7**, and **Table 1**. **Figure S7** shows the XPS survey spectra of rGO@3D-Cu and of the GO precursor. Per **Table 1**, the atomic ratio of C 1s : O 1s in GO precursor is 2.1, while this ratio increases to 3.0 for rGO@3D-Cu. **Figure 1(g)** shows the XPS core level spectra of C 1s and O 1s for rGO@3D-Cu and GO precursor. For GO precursor, the C 1s peak can be fitted into four separated peaks of C=C/C-C/C-H (284.5 eV), C-O (epoxy/hydroxyl, 286.5 eV), C=O (288.3 eV), and O=C-O (289.9 eV).[30, 33] After coating the content of C-O group in rGO@3D-Cu decreases from 40.5 at.% to 30.6 at.%. Oxygen functional groups, associated defects, and an overall negatively charged surface have been reported to promote Li wetting.[34] It has also been shown that with Li, thermal wetting and electrochemical wetting follow similar trends.[35] A comparable similarity in thermal and electrochemical wetting behavior should exist for K. It will be demonstrated that in the context of the negligible wetting of molten K on bare 3D-Cu, oxygen functional groups are in-fact essential.

Table 1. XPS-derived atomic content of C and O chemical groups in rGO@3D-Cu and in the GO precursor.

Sample	Atomic ratio of C 1s / O 1s	C 1s group content (at%) – BE (eV)				O 1s group content (at%)		
		C=C	C-O	C=O	O=C-O	C-O	C=O	O=C-O
rGO@3D-Cu	3.0	60.8 (284.5)	30.6 (286.3)	7.0 (288.3)	1.6 (290.0)	79.8 (532.5)	17.1 (531.8)	3.1 (531.0)
GO	2.1	51.5 (284.5)	40.5 (286.5)	7.5 (288.3)	0.5 (289.9)	85.7 (532.8)	13.2 (532.1)	1.1 (531.4)

Figure 2 shows photographs that demonstrate the major enhancement of the K wetting behavior (*i.e.* potassiophilicity) by the rGO coating. The poor wetting achieved with the baseline 3D-Cu is also shown as the bottom row. In that case, no wetting is achieved even at 160 seconds of immersion in the bath or afterward. For rGO@3D-Cu, after 6 seconds the molten K has been completely and uniformly thermally infused into rGO@3D-Cu. A video highlighting the entire process for rGO@3D-Cu and baseline 3D-Cu can be found in **Movies S1** and **S2**. The above observations reveal that rGO@3D-Cu is potassiophilic, a result that directly transfers to the electrochemical tests. Potassiophilicity is correlated with substrate - molten metal interface energy and can be furthermore correlated to the morphology of film growth *via* classic growth models.[36] The three models are the two-dimensional (2D) layer-by-layer mode (Frank–van-der-Merwe, F–M mode), three-dimensional (3D) island mode (Volmer–Weber, V–W mode), and 2D layer followed by 3D island mode (Stranski–Krastanov, S–K mode). The type of growth that occurs is a balance between substrate surface energy γ_s, growing film surface energy γ_f and the energy of their interface γ_{sf}.

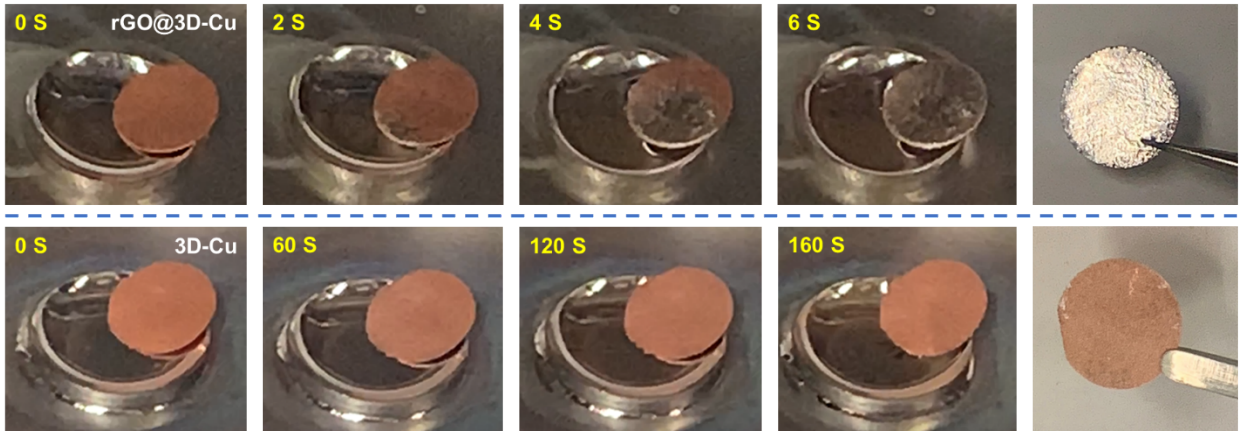

Figure 2. Photographs demonstrating the major enhancement of the K wetting behavior (i.e. potasiophilicity) of the 3D-Cu surface by the rGO coating vs. the poor wetting achieved with the baseline 3D-Cu. The molten K being held at 300 °C inside the glove box with the copper being dipped into it.

The Frank van der Merwe (F-M), Volmer Weber (V-W), and Stranski-Krastanov (S-K) modes for thin film growth are well-established in vacuum deposition literature.[37] Although these models were aimed at capturing the phenomenology of vapor - solid film growth, an electrochemical

plating analog should be applicable,[38] with the caveat that the film's surface contacts the SEI rather than vacuum. The F-M, V-W and S-K growth modes may be viewed as a competition between surface forces, described by Young's equation. The surface tensions balance at point: $\gamma_{sf} + \gamma_f \cos\theta = \gamma_s$, where γ_{fs} is the film - substrate surface tension, γ_f is the film surface tension, and γ_s is the substrate surface tension. This straightforward force balance then establishes the thermodynamic shape of a film on a substrate, as described by its wetting angle: $\cos\theta = (\gamma_s - \gamma_{fs})/\gamma_f$. When the inequality $\gamma_s - \gamma_{fs} \geq \gamma_f$ is satisfied, a wetting angle of 0° is obtained. This is an ideal case realization of F-M growth mode, with fully wetted planar thin film growth. As the inequality $\gamma_s - \gamma_{fs} < \gamma_f$ increases, the film no longer perfectly wets the substrate. At a certain non-zero wetting angle there is a transition to V-W growth mode, and the film exists as isolated islands on the substrate. The S-K growth mode can be realized if there are changes to the surface tensions as a function of film thickness, *e.g.* due to accumulation of strain energy causing a rise in γ_{fs}. In the classic view of S-K, a film will remain planar (wetted) at the substrate interface but forms islands away from the substrate as it thickens. It is also possible that island growth fully transitions to planar or *vise versa* due to chemical or electrochemical reactions that alter the surface tensions. For electrodeposition, there is the complexity that in addition to the equilibrium surface energies, there is a significant kinetic effect in the form of nucleation overpotentials.[39, 40] When the nucleation overpotential is large, the deposition is usually under mixed diffusion/kinetic control, and radial transport of metal ions in bulk solution results in the formation of islands, similar to the V-W mode. Therefore, a small overpotential is beneficial to the formation of a uniform plated film.

Figure 3 presents a comparison of the galvanostatic cycling results for rGO@3D-Cu and for planar Cu baseline. **Figures 3(a) - (c)** show asymmetric half-cells, and while **(d) - (i)** show symmetric cells. In each row, the smaller second and third panels are the enlarged profiles of marked regions in the first larger panel. The half-cell voltage-time profiles for the baseline 3D-Cu and rGO@Cu are shown in **Fig. S8**, presented identically. All half-cells were tested with no "extra" K reservoir being employed. Since the Coulombic efficiency (CE) was not 100%, an anodic voltage cutoff of 1 V was employed, after which point the current is reversed. **Figures 3(a) – (c)** show the half-cell voltage-time profiles of rGO@3D-Cu and Cu. Each plating cycle corresponds to a current density 0.5 mA cm^{-2} for one hour, with stripping being terminated at 1 V cutoff. Higher

current density results for rGO@3D-Cu are shown in **Fig. S9**, with the plating current being 1 mA cm^{-2} for 30 mins. **Figure S10** shows the first five-cycle formation cycling profiles of rGO@3D-Cu, 3D-Cu, rGO@Cu, and Cu. The symmetric cells of rGO@3D-Cu // rGO@3D-Cu were assembled using two identical molten K infused rGO@3D-Cu electrodes, analogous to the one shown in **Fig. 2**. The symmetric Cu // Cu cells were assembled using bare K foil joined to planar Cu current collector, the same approach used for the counter electrodes in the half-cells. Those results are shown in **Figs. 3(d) - (i)**. For the symmetric cells, the current density and time for each plating versus stripping cycle are same.

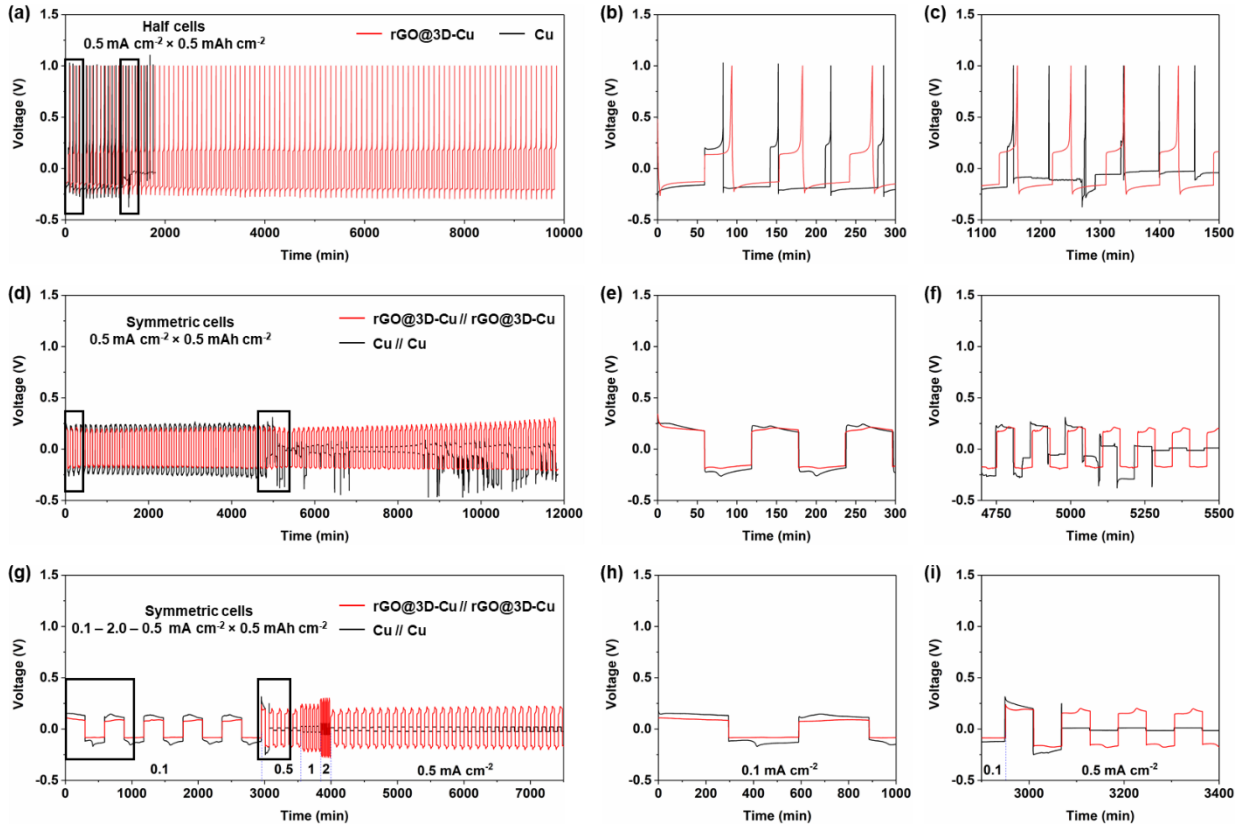

Figure 3. Electrochemical performance comparison, showing the galvanostatic K plating – stripping profiles at various current densities. **(a) - (c)** Electrochemically infused rGO@3D-Cu in "half-cell" configuration, with baseline planar Cu. The results for 3D-Cu and rGO@Cu are shown in the supplemental, along with more data for rGO@3D-Cu. **(d) – (i)** Thermally infused symmetric rGO@3D-Cu // rGO@3D-Cu, with baseline Cu // Cu. The current densities and capacity achieved per cycle are labeled directly on panels **(a)**, **(d)** and **(g)**. Panels **(b),(c), (e),(f) and (h),(i)** being enlarged profiles of marked regions in **(a)**, **(d)** and **(g)**, respectively.

Significant differences in the voltage-time profiles of rGO@3D-Cu *vs.* the baselines were observed, both in the half-cells (3D-Cu, rGO@Cu and planar Cu) and in symmetric cells (planar Cu). Both rGO@3D-Cu and rGO@3D-Cu // rGO@3D-Cu exhibit stable plating and striping at up to 10,000 minutes, corresponding to 100 cycles. On the other end of the spectrum is the planar Cu, which is neither stable as a half-cell nor as a symmetric cell. For example, for the half-cell Cu (**Fig. 3(a) - (c)**) it may be observed that after 17th cycle (1,150 mins) there was minimal capacity stripped at each cycle. Prior to the electrode finally shorting, it approached an ideally polarizable electrode, indicating a severe impedance rise. In fact, for the Cu foil, the voltage-time profile begins to substantially deteriorate from the 15th cycle (1,101 mins) onward. Although the cycling performance of 3D-Cu and rGO@Cu are improved as compared to the Cu foil, both are still inferior to the rGO@3D-Cu. The 3D-Cu sample approaches an ideally polarizable electrode after 54 cycles (5,110 mins). At that point there is minimal capacity stripped. For rGO@Cu this occurs after 35 cycles, corresponding to 2,760 minutes, followed by electrical shorting as manifested in the plating and stripping overpotentials suddenly approaching zero. One important difference between failure of 3D-Cu vs. rGO@Cu is that for the former, there is no observable shorting. This indicates that despite it being inferior to rGO@3D-Cu, the 3D-Cu architecture is still effective in preventing dendrite penetration across the separator. Both the Cu and the rGO@Cu ultimately do suffer electrical shorting, indicating that a potassiophilic surface by itself does not offer sufficient protection.

For the rate performance of symmetric cells, the testing protocol was the following: 0.1 mA cm^{-2} from 1 to 5 cycle, 0.5 mA cm^{-2} from 6 to 10 cycle, 1 mA cm^{-2} from 11 to 15 cycle, 2 mA cm^{-2} from 16 to 20 cycle, and then back to 0.5 mA cm^{-2} from 21 to 50 cycle. According to **Figs. 3(d) - 3(f)**, there is a major difference in the electrochemical stability of rGO@3D-Cu // rGO@3D-Cu *vs.* Cu // Cu when tested 0.5 mA cm^{-2} to achieve 0.5 mAh cm^{-2} capacity per cycle. There is likewise a major difference between the two when tested at 0.1 – 0.5 mA cm^{-2} to achieve 0.5 mAh cm^{-2} per cycle. Those results are shown in **Figs. 3(g) - 3(i).** The rGO@3D-Cu // rGO@3D-Cu exhibits stable plating/striping at 0.5 mA cm^{-2} up to and including 100 cycles. For Cu // Cu, it may be observed that after 45 cycles (5,160 minutes) there is cell failure, first in the form of an overpotential rise and CE fall, followed by electrical shorting. The rGO@3D-Cu // rGO@3D-Cu

can sustain a current density of up to 2 mA cm^{-2} without instability or shorts. When the current density is then turned down to 0.5 mA cm^{-2}, the sample keeps cycling in a stable manner. By contrast, when the current density increases from 0.1 mA cm^{-2} to 0.5 mA cm^{-2}, the Cu // Cu symmetric cell fails. **Table S1** shows a comparison of the electrochemical performance rGO@3D-Cu and rGO@3D-Cu // rGO@3D-Cu versus state-of-the-art potassium metal anodes previously published. It may be observed that the overall electrochemical performance of half-cell rGO@3D-Cu and of rGO@3D-Cu // rGO@3D-Cu are quite favorable relative to the limited number of K metal anode publications in the literature both with ether - based and carbonate - based electrolytes.

The trends in the galvanostatic results can be understood in a more quantitative manner through analysis of the associated overpotentials. Dendrite growth occurs during plating with that overpotential then being associated with K^+ ion diffusion through SEI, nucleation barriers, growth stresses, *etc*.[41] It is believed that "dead metal" formation occurs rather at stripping, due to preferential dissolution of the dendrite at its base. The plating - stripping overpotentials do not need to be symmetric, since the processes may not follow the same kinetic path. For instance, preferential plating may occur onto pre-existing dendrites, whereas stripping may be more uniform, or *vise-versa*. **Figures 4(a) - 4(c)** show the half-cell data, while **4(d) - 4(f)** show the symmetric cell data, the results being calculated from the 0.5 mA cm^{-2} profiles. The plating and the stripping overpotentials for rGO@3D-Cu, 3D-Cu, rGO@Cu and Cu are shown in **Figs. 4(b**) and **4(c)**, respectively. The first cycle plating and stripping profiles for the two extreme cases, rGO@3D-Cu and Cu, are shown in **Fig. 4(a)**. The first cycle plating and stripping profiles of rGO@3D-Cu // rGO@3D-Cu and Cu // Cu are shown in **Fig. 4(d)**. The plating and the stripping overpotentials of these symmetric cells are shown in **Figs. 4(e**) and **4(f)**.

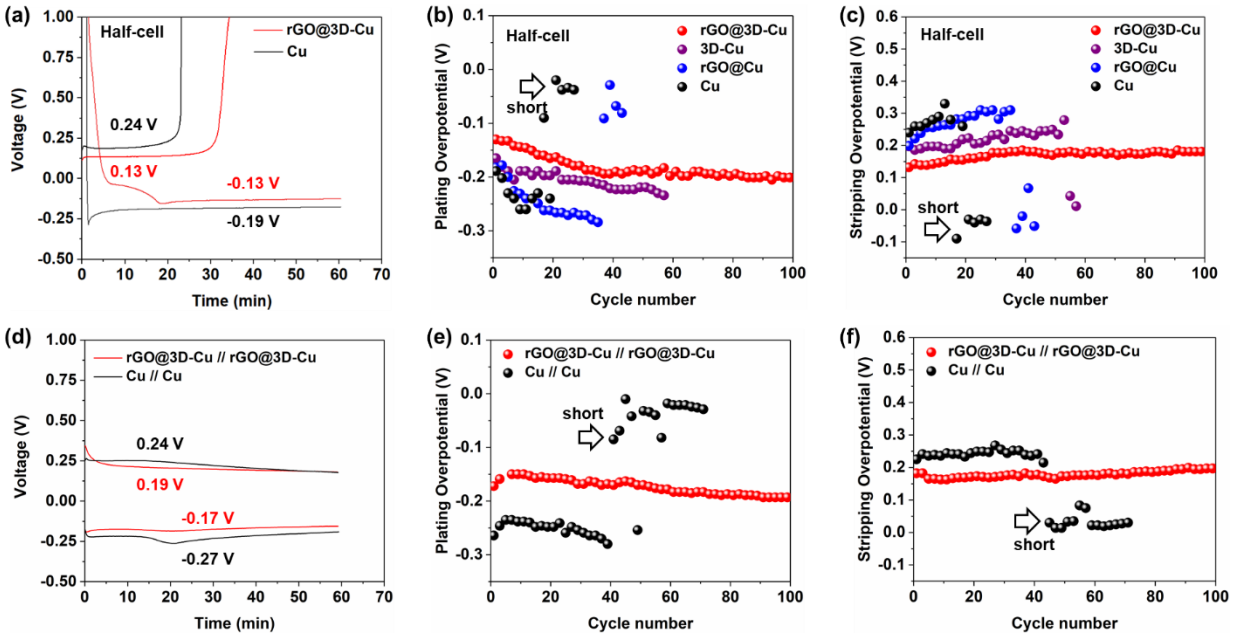

Figure 4. Electrochemical analysis for half-cells and for symmetric cells, analysis being performed on the 0.5 mA cm^{-2} profiles. **(a)** Comparison of the first plating profile for rGO@3D-Cu and baseline Cu. **(b)** Comparison of the plating overpotential for rGO@3D-Cu, 3D-Cu, rGO@Cu and Cu. **(c)** Comparison of the stripping overpotential for these half-cells. **(d)** Comparison of the first plating profile for rGO@3D-Cu // rGO@3D-Cu and baseline Cu // Cu. **(e)** and **(f)** Comparison of the plating and stripping overpotentials for these symmetric cells.

Per **Fig. 4(a)** the plating overpotential of rGO@3D-Cu and Cu baseline are -0.13 V and -0.19 V, respectively. The stripping overpotential of rGO@3D-Cu and Cu baseline are 0.13 V and 0.24 V, respectively. The rGO@3D-Cu exhibits a much smaller overpotential in both plating or stripping, which signals that growth should be planar, rather than island-like.[37, 39] Throughout cycling, the rGO@3D-Cu shows the smallest overpotentials and the best voltage stability. After 40 cycles (~3,750 mins), its plating and stripping overpotential is stable at -0.19 V and 0.18 V, respectively. By contrast, the Cu baseline shows the most violent oscillation in voltage prior to the earliest failure. For example, the plating overpotential of Cu is at -0.26 V at 9 cycles (640 mins). Then, the plating overpotential drops to -0.088 V at 17 cycles (1,150 mins), the value being -0.024 V at 20 cycles (1,410 mins). A similar trend occurs for the stripping overpotential: The stripping overpotential of Cu first rapidly increases to 0.331 V at 13 cycles (945 mins), then decreases to -0.87 V at 17 cycles, and finally approaches zero (-0.02 V) at 20 cycles prior to cell failure. The

initial plating and stripping overpotential for 3D-Cu is -0.165 V and 0.197 V, respectively, with likewise fluctuation. A fast increase is observed after 50 cycles (4,740 mins), hitting -0.23 V at 54 cycles (5,110 mins). A similar trend occurs for the stripping overpotential. The stripping overpotential of 3D-Cu first fast increases to 0.28 V at 52 cycles (4,940 mins), then sharply decreases close to zero after 54 cycles, prior to cell failure. The initial plating and stripping overpotential of rGO@Cu is -0.182 V and 0.199 V, respectively. Early in the cycling, the plating overpotential increases to -0.28 V at 36 cycles (2,830 mins). Then it decreases to -0.029 V at 39 cycles (3,012 mins) followed by failure. A similar trend occurs for the stripping overpotentials. The stripping overpotential of rGO@Cu first increases to 0.314 V after 35 cycles (2,760 mins), and then decreases to close to zero (-0.02 V) after 39 cycles, followed by failure.

Per **Fig. 4(d)** the cycle 1 plating overpotentials of rGO@3D-Cu // rGO@3D-Cu and Cu // Cu are -0.17 V and -0.27 V, respectively. The cycle 1 stripping overpotentials of rGO@3D-Cu // rGO@3D-Cu and Cu // Cu are 0.19 V and 0.24 V, respectively. Throughout cycling this trend continues. After 50 cycles (5,880 mins), the rGO@3D-Cu // rGO@3D-Cu plating and stripping overpotentials are stable at -0.18 V and 0.19 V. By contrast, the Cu // Cu baseline shows a sharply increasing voltage oscillation profile prior to failure. For example, the plating overpotential of Cu // Cu increases to -0.28 V at 39 cycles (4,520 mins). At shorting near 41 cycles (4,800 mins) the plating overpotential drops to -0.085 V, and then to effectively zero (-0.01 V) at cycle 45 (5,280 mins). A similar trend occurs for the stripping overpotential: It rapidly increases to 0.268 V at 27 cycles (3,120 mins), and then decreases to 0.03 V at 45 cycles.

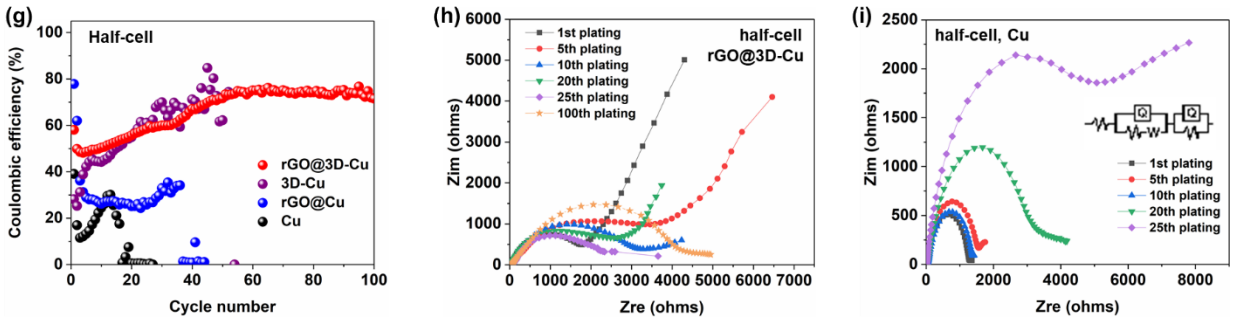

Figure 4. cont. **(g)** Comparison of Coulombic efficiency (CE) of the half-cells. The CE value of the symmetric cells was ~99.99% due to the large K reservoir on each side. **(h)** and **(i)** EIS Nyquist plots of rGO@3D-Cu and Cu half-cells, which represent the two extremes of favorable versus poor performance.

The Coulombic efficiency (CE) in half-cells is considered a key descriptor for a stable versus unstable metal anode. A stable value of CE has been directly correlated with a stable SEI and with lack of dendritic growth.[42] For symmetric cells where there is an effectively infinite K reservoir on each side, causing the CE values to be near 100%. Hence, the presented CE analysis is for the half-cells, where there is no K reservoir. As shown in **Fig. 4(g)**, the baseline Cu foil shows a rapid decay in its CE values. After about 17 cycles, the CE of the Cu foil approaches zero, indicating that the majority of the K metal is not recovered upon the stripping cycle. Limited plating and stripping do keep occurring presumably at the pre-existing dendrites. This rapidly leads to a cell electrical short, per the overpotential results. For 3D-Cu, the CE decays rapidly after 54 cycles (5,110 mins) although the cell does not short. For rGO@Cu, its CE is below 40% after 36 cycles followed by a short. The rGO@3D-Cu shows a relatively stable CE that gradually increases with cycling, reaching 72% by cycle 50, reaching a maximum value of 76% in the following cycles. By comparison, prior K-metal cycling results in a carbonate electrolyte achieved a maximum CE value of 50%.[14] For rGO@3D-Cu it may be observed that up to around cycle 50, the CE values steadily increase. After which point the CE remains stable up to and including cycle 100. This effect is likely a manifestation of real cycling-induced changes in the SEI structure, leading to more facile diffusion of K^+ through the SEI layer, lower SEI resistance, *etc*. Improved CE at early stage cycling is observed for all the specimens to a varying extent, indicating a general phenomenon that needs to be understood further.

Electrochemical impedance spectroscopy (EIS) analysis for the two extreme cases, rGO@3D-Cu and Cu foil was conducted at different plating/stripping cycles. The EIS tests were performed in the fully plated state at open-circuit voltage. The associated Nyquist plots are shown in **Figs. 4(h)** and **4(i)**, with the associated fits being shown in **Table 2.**

Table 2. EIS Impedance values for rGO@3D-Cu and Cu foil during cycling.

Cycling	R_{CT} for Cu foil	R_{SEI} for Cu foil	R_{SEI+CT} rGO@3D-Cu
1st plating	1091 Ohms	25 Ohms	1975 Ohms
5th plating	1400	63	2906

10th plating	1157	197	2310
20th plating	2775	1738	2154
25th plating	4396	6167	1903
100th plating	N/A	N/A	2865

The impedance value R_{CT} is the charge transfer resistance. It accounts for resistance between the current collector and the K metal and the resistance of SEI film-electrolyte interface.[43] The impedance value R_{SEI} corresponds to solid electrolyte interphase, which is itself a complex composite of organic and inorganic phases.[44] For systems with high impedance such as the baseline Cu, the R_{CT} and R_{SEI} are prominent enough that they be mathematically deconvoluted. For the much less resistive rGO@3D-Cu the two semicircles overlap and therefore can't be distinguished. Therefore an impedance nomenclature of R_{SEI+CT} is employed for rGO@3D-Cu, and a single semicircle is used for fitting. For the Cu foil, when the cycle number is increased from 1 to the terminal 25 (last cycle before failure), R_{CT} increases from 1,091 Ohms to 4,396 Ohms. The R_{SEI} values increase from 25 Ohms to 6,167 Ohms. This indicates that a thick SEI layer is formed. The SEI is both a root cause for dendrite growth,[4, 44] and a secondary outcome dendrite formation,[45] the SEI-dendrite negative synergy being self-amplifying. Conversely, the R_{SEI+CT} impedance of rGO@3D-Cu is quite stable throughout cycling, ending at 2,865 Ohms at cycle 100. The slight decrease in the R_{SEI+CT} values at cycle 20 and 25 may be a mathematical fitting effect. It may also be another manifestation (in addition to improved CE at comparable cycle numbers) of a change in the SEI structure.

Figure 5 shows top-down SEM images of the fully plated electrode surfaces conducted at different plating/stripping times (cycles). The rGO@3D-Cu specimen was again compared to its most opposite in performance, namely planar Cu. **Figures 5(a) – (c)** show with increasing magnification the top-down SEM images of rGO@3D-Cu, plated at cycle 1. **Figures 5(d) – (f)** show these results for Cu, also plated at cycle 1. **Figures 5(g) – (i)** show rGO@3D-Cu, plated at cycle 100, while **(j) – (l)** show rGO@3D-Cu, stripped at cycle 100. Finally, **Figs. 5(m) – (o)** show the baseline Cu, plated at cycle 20. For the rGO@3D-Cu current collectors, the plated K metal is conformal to the current collector even at cycle 100. There is no evidence of morphologically distinct dendrites that protrude from the overall growing front. The post 100 cycles stripped rGO@3D-Cu specimen does not show evidence of dead K, at least not of anything that resembles

a dendrite of any morphology. Conversely, the baseline Cu is full of crystallographic branched K dendrites by cycle 20. While being aesthetically attractive, there is no doubt that these flower-like growths are a manifestation of the interfacial instability in the form of severe SEI growth. They are also the root cause of additional SEI formation during cycling. Even at cycle 1, there is evidence for non-uniform and crystallographically oriented growth of K crystals, as evidenced by the highest magnification image in **Fig. 5(f).**

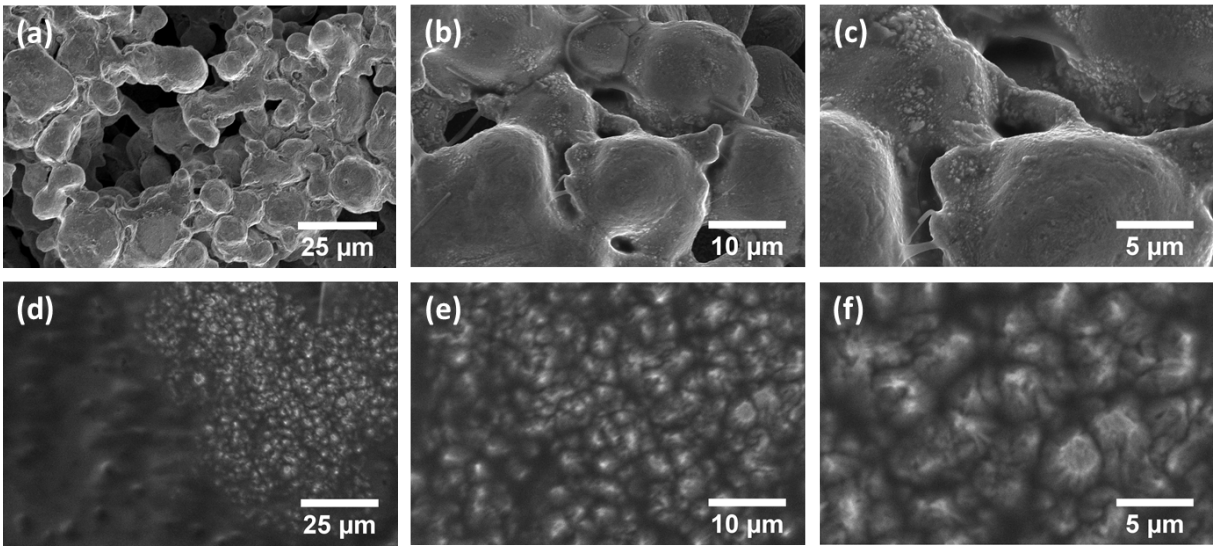

Figure 5. Post-cycled morphology observation for half-cells of rGO@3D-Cu and planar Cu baseline, taken by top-down SEM. **(a) – (c)** rGO@3D-Cu, plated at cycle 1, shown with increasing magnification. **(d) – (f)** baseline Cu, plated at cycle 1.

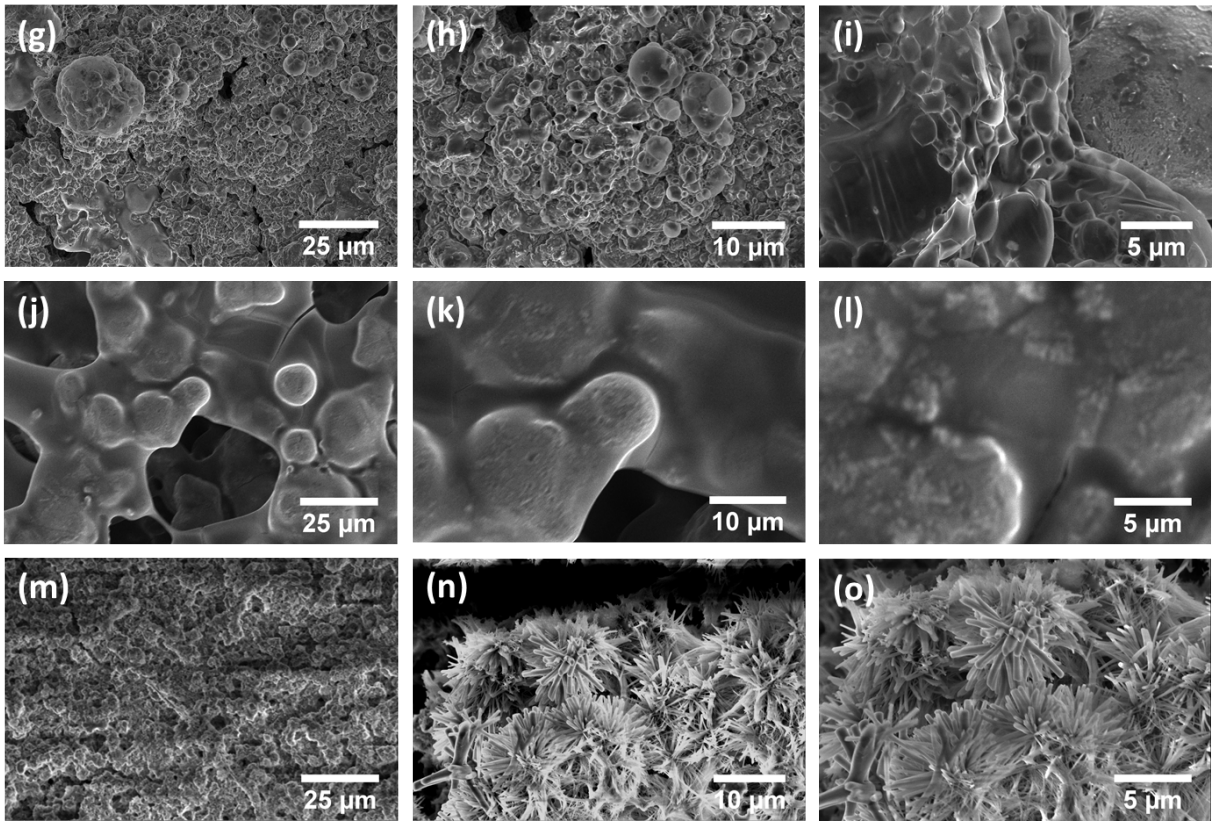

Figure 5. cont. **(g) – (i)** rGO@3D-Cu, plated at cycle 100. **(j) – (l)** rGO@3D-Cu, stripped at cycle 100. **(m) – (o)** baseline Cu, plated at cycle 20.

Schematic 2 shows a mechanistic illustration of K plating/stripping behavior on rGO@3D-Cu versus the baseline planar Cu. The complex "flower-like" branched morphologies observed on the Cu may be attributed to secondary nucleation on pre-existing dendrites during ongoing plating. The pre-existing dendrites are remnants that are not stripped during the previous cycle, as indicated by the very low measured CE for the baseline Cu. During stripping, while some dendrites become isolated as "dead metal", others retail electrical contact with the current collector. Their inability to be fully dissolved may rather be a kinetic effect, caused by severe SEI formation. The end-of life galvanostatic profiles and the EIS results supports this scenario; plating and stripping is extremely difficult due to the impedance rise. Excessive SEI growth kinetically hinders K^+ transport, preventing even the electrically connected portions of the metal front from dissolving before the cutoff voltage is reached. Such asymmetric stripping - plating behavior leads to the ultimate dendrite-induced electrical shorts observed in Cu and rGO@Cu half-cells and the Cu // Cu symmetric cells.

The rGO@3D-Cu substrate combines chemical effects with geometrical effects to suppress dendrite growth and maintain stable cycling. The rGO@Cu and 3D-Cu cycling data demonstrate that while the chemical or the geometrical effects do improve performance, it is their synergy that is the most effective. Interfacial and surface tension considerations in dictating the mode of thin film growth (F-M, V-W, S-K) can explain the differences between rGO@3D-Cu vs. 3D-Cu, or rGO@Cu vs. Cu. From the earlier discussion, it may be concluded that a good strategy to promote planar growth during metal plating is to reduce the γ_{fs}, *i.e.* to transition from a potassiophobic interface to a potassiophilic one. The K metal is very reactive with O/OH groups, thereby leading to a reduction in γ_{fs} over the baseline Cu. An increase in the surface tension of the substrate γ_s would also be effective in promoting more planar growth during plating. A chemically active rGO surface full of structural defects and O/OH groups possess higher surface tension (higher energy) as compared to the baseline Cu. Improved thermal or electrochemical wetting also means that a higher number of initial K metal nuclei will be formed. Nucleating a K film composed of dense continuous distribution of nuclei, rather than a coarser array of isolated islands is a self-reinforcing feature for growth stability during later stages of plating. From the start, there is a lower effective current density, as well as a large number of competing nuclei that advance in parallel. Hence, early wetting behavior is one key attribute necessary for stable cycling of K metal. However, as shown by the premature failure of rGO@Cu, tuning of the interfacial tension is not enough by itself.

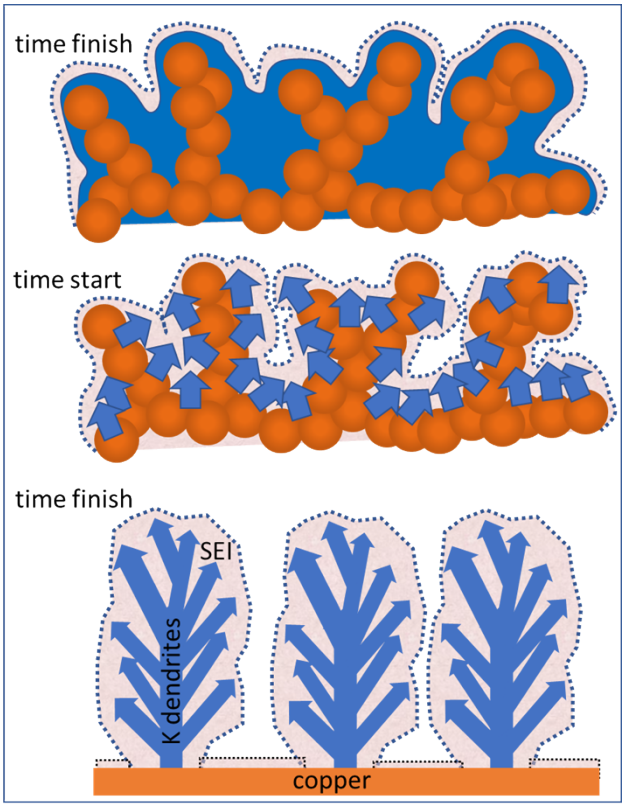

Schematic 2. Mechanistic illustration of K plating/stripping behavior of rGO@3D-Cu versus the planar Cu current collector.

The role of the approximately twenty times higher surface area 3D-Cu vs. planar Cu is to reduce the effective current density during plating/stripping. This is well-known to promote planar, rather than dendritic growth. The surface of 3D-Cu is macroscopically rough and tortuous. It is therefore expected that dendrite growth is further suppressed though geometrical frustration: On a planar support, the K nuclei are co-planar and will grow parallel to each other without steric hinderance. This is not the case when the current collector is roughened and the nuclei form on all the electrolyte exposed surfaces. On 3D-Cu, the early-stage K crystallites will be non-coplanar and will physically interfere during subsequent growth. This would be another factor in reducing the formation of dendrites during cycling. Interestingly, the 3D-Cu is more electrochemically stable than rGO@Cu, including being resistant to dendrite penetration. One implication of this result is that at later stages of growth, interfacial - energy effects become less important than geometrical effects. It may actually be found that after a number of cycles, or after a certain capacity per cycle,

K metal growth on both Cu and rGO surfaces transitions to Stranski–Krastanov mode. This may be correlated with emergence of dendrites. At that point, geometrical effects in providing steric hinderance become crucial to prevent shorting. The observation that 3D-Cu fails by impedance rise rather than electrical shorting supports this conclusion. According to the electrochemical cycling results presented, it is evident that rGO@3D-Cu synergizes the interfacial/surface tension and the geometrical effects. The result is a substantially more favorable electrochemical performance (voltage stability, CE) over the electrodes that employ one or the other attribute only.

Acknowledgements

D.M. (research conception and guidance, manuscript preparation), P.L. and Y.W. (synthesis, electrochemical analysis) were supported by the U.S. Department of Energy, Office of Basic Energy Sciences, Division of Materials Sciences and Engineering under Award # DE-SC0018074. SEM analysis was performed (J.W.) at the Center for Integrated Nanotechnologies, an Office of Science User Facility operated for the U.S. Department of Energy (DOE) Office of Science. Los Alamos National Laboratory, an affirmative action equal opportunity employer, is managed by Triad National Security, LLC for the U.S. Department of Energy's NNSA, under contract 89233218CNA000001. J.N. (Raman spectroscopy and electrochemical evaluation) is supported by Energy Storage Program, Office of Electricity, Department of Energy.

References

[1] a) J. B. Goodenough, *Acc Chem Res* **2013**, *46*, 1053; b) A. Eftekhari, Z. Jian, X. Ji, *ACS Appl Mater Interfaces* **2017**, *9*, 4404; c) J. Liu, Z. Bao, Y. Cui, E. J. Dufek, J. B. Goodenough, P. Khalifah, Q. Li, B. Y. Liaw, P. Liu, A. Manthiram, Y. S. Meng, V. R. Subramanian, M. F. Toney, V. V. Viswanathan, M. S. Whittingham, J. Xiao, W. Xu, J. Yang, X.-Q. Yang, J.-G. Zhang, *Nature Energy* **2019**, *4*, 180; d) A. Eftekhari, D.-W. Kim, *Journal of Power Sources* **2018**, *395*, 336.

[2] a) D. Larcher, J. M. Tarascon, *Nat Chem* **2015**, *7*, 19; b) Y. Wang, X. Fu, M. Zheng, W. H. Zhong, G. Cao, *Adv Mater* **2019**, *31*, e1804204; C. c) Vaalma, D. Buchholz, M. Weil, S. Passerini, *Nature Reviews Materials* **2018**, *3*, 18013; d) M. D. Tikekar, S. Choudhury, Z. Tu, L. A. Archer, *Nature Energy* **2016**, *1*, 16114; e) R. Zhang, N. W. Li, X. B. Cheng, Y. X. Yin, Q. Zhang, Y. G. Guo, *Adv Sci (Weinh)* **2017**, *4*, 1600445; f) Y. Zhao, K. R. Adair, X. Sun, *Energy & Environmental Science* **2018**, *11*, 2673; g) R. Cao, W. Xu, D. Lv, J. Xiao, J.-G. Zhang, *Advanced Energy Materials* **2015**, *5*,

1402273; h) Y. Shao, F. Ding, J. Xiao, J. Zhang, W. Xu, S. Park, J.-G. Zhang, Y. Wang, J. Liu, *Advanced Functional Materials* **2013**, *23*, 987; i) C. Zhao, L. Liu, X. Qi, Y. Lu, F. Wu, J. Zhao, Y. Yu, Y.-S. Hu, L. Chen, *Advanced Energy Materials* **2018**, *8*, 1703012; j) X. Hong, J. Mei, L. Wen, Y. Tong, A. J. Vasileff, L. Wang, J. Liang, Z. Sun, S. X. Dou, *Adv Mater* **2019**, *31*, e1802822; k) J. Y. Hwang, S. T. Myung, Y. K. Sun, *Chem Soc Rev* **2017**, *46*, 3529.

[3] a) D. Lin, Y. Liu, Y. Cui, *Nat Nanotechnol* **2017**, *12*, 194; b) X. B. Cheng, R. Zhang, C. Z. Zhao, Q. Zhang, *Chem Rev* **2017**, *117*, 10403.

[4] B. Lee, E. Paek, D. Mitlin, S. W. Lee, *Chem Rev* **2019**, 10.1021/acs.chemrev.8b00642.

[5] H. Wang, D. Yu, C. Kuang, L. Cheng, W. Li, X. Feng, Z. Zhang, X. Zhang, Y. Zhang, *Chem* **2019**, *5*, 313.

[6] A. Eftekhari, *ACS Sustainable Chemistry & Engineering* **2019**, *7*, 5602.

[7] a) W. Zhang, Y. Liu, Z. Guo, *Sci Adv* **2019**, *5*, eaav7412; b) Y. Wu, H. B. Huang, Y. Feng, Z. S. Wu, Y. Yu, *Adv Mater* **2019**, 10.1002/adma.201901414, e1901414.

[8] S. Komaba, T. Hasegawa, M. Dahbi, K. Kubota, *Electrochemistry Communications* **2015**, *60*, 172.

[9] K. Kubota, M. Dahbi, T. Hosaka, S. Kumakura, S. Komaba, *Chem Rec* **2018**, *18*, 459.

[10] K. Chihara, A. Katogi, K. Kubota, S. Komaba, *Chem Commun (Camb)* **2017**, *53*, 5208.

[11] A. Eftekhari, *ACS Sustainable Chemistry & Engineering* **2018**, *7*, 3684.

[12] a) L. Li, S. Basu, Y. Wang, Z. Chen, P. Hundekar, B. Wang, J. Shi, Y. Shi, S. Narayanan, N. Koratkar, *Science* **2018**, *359*, 1513; b) K. R. Adair, C. Zhao, M. N. Banis, Y. Zhao, R. Li, M. Cai, X. Sun, *Angew Chem Int Ed Engl* **2019**, 10.1002/anie.201907759; c) H. Yadegari, X. Sun, *Acc Chem Res* **2018**, *51*, 1532; d) Y. Zhao, L. V. Goncharova, A. Lushington, Q. Sun, H. Yadegari, B. Wang, W. Xiao, R. Li, X. Sun, *Adv Mater* **2017**, *29*, 1606663.

[13] S. Xia, X. Wu, Z. Zhang, Y. Cui, W. Liu, *Chem* **2019**, *5*, 753.

[14] N. Xiao, W. D. McCulloch, Y. Wu, *J Am Chem Soc* **2017**, *139*, 9475.

[15] W. Zhang, W. K. Pang, V. Sencadas, Z. Guo, *Joule* **2018**, *2*, 1534.

[16] N. Xiao, G. Gourdin, Y. Wu, *Angew Chem Int Ed Engl* **2018**, *57*, 10864.

[17] Y. Li, L. Zhang, S. Liu, X. Wang, D. Xie, X. Xia, C. Gu, J. Tu, *Nano Energy* **2019**, *62*, 367.

[18] Y. Gu, W. W. Wang, Y. J. Li, Q. H. Wu, S. Tang, J. W. Yan, M. S. Zheng, D. Y. Wu, C. H. Fan, W. Q. Hu, Z. B. Chen, Y. Fang, Q. H. Zhang, Q. F. Dong, B. W. Mao, *Nat Commun* **2018**, *9*, 1339.

[19] L. Qin, Y. Lei, H. Wang, J. Dong, Y. Wu, D. Zhai, F. Kang, Y. Tao, Q. H. Yang, *Advanced Energy Materials* **2019**, *9*, 1901427.

[20] Y. Ding, X. Guo, Y. Qian, L. Zhang, L. Xue, J. B. Goodenough, G. Yu, *Adv Mater* **2019**, *31*, e1806956.

[21] L. Xue, H. Gao, W. Zhou, S. Xin, K. Park, Y. Li, J. B. Goodenough, *Adv Mater* **2016**, *28*, 9608.

[22] L. Zhang, X. Xia, Y. Zhong, D. Xie, S. Liu, X. Wang, J. Tu, *Adv Mater* **2018**, *30*, e1804011.

[23] a) Z. Tu, P. Nath, Y. Lu, M. D. Tikekar, L. A. Archer, *Acc Chem Res* **2015**, *48*, 2947; b) M. D. Tikekar, S. Choudhury, Z. Tu, L. A. Archer, *Nature Energy* **2016**, *1*, 16114; c) X. Yu, A. Manthiram, *Energy & Environmental Science* **2018**, *11*, 527.

[24] T. Hosaka, S. Muratsubaki, K. Kubota, H. Onuma, S. Komaba, *J Phys Chem Lett* **2019**, 10.1021/acs.jpclett.9b00711.

[25] a) H. Che, S. Chen, Y. Xie, H. Wang, K. Amine, X.-Z. Liao, Z.-F. Ma, *Energy & Environmental Science* **2017**, *10*, 1075; b) W. Chen, T. Lei, C. Wu, M. Deng, C. Gong, K. Hu, Y. Ma, L. Dai, W. Lv, W. He, X. Liu, J. Xiong, C. Yan, *Advanced Energy Materials* **2018**, *8*, 1702348; c) K. Xu, *Chem Rev* **2014**, *114*, 11503.

[26] X. Cao, D. Qi, S. Yin, J. Bu, F. Li, C. F. Goh, S. Zhang, X. Chen, *Adv Mater* **2013**, *25*, 2957.

[27] D. Qi, Z. Liu, Y. Liu, W. R. Leow, B. Zhu, H. Yang, J. Yu, W. Wang, H. Wang, S. Yin, X. Chen, *Adv Mater* **2015**, *27*, 5559.

[28] K. Krishnamoorthy, M. Veerapandian, K. Yun, S. J. Kim, *Carbon* **2013**, *53*, 38.

[29] a) J. Zhang, H. Yang, G. Shen, P. Cheng, J. Zhang, S. Guo, *Chem Commun (Camb)* **2010**, *46*, 1112; b) O. Akhavan, *Carbon* **2010**, *48*, 509.

[30] a) S. Stankovich, D. A. Dikin, R. D. Piner, K. A. Kohlhaas, A. Kleinhammes, Y. Jia, Y. Wu, S. T. Nguyen, R. S. Ruoff, *Carbon* **2007**, *45*, 1558; b) D. Yang, A. Velamakanni, G. Bozoklu, S. Park, M. Stoller, R. D. Piner, S. Stankovich, I. Jung, D. A. Field, C. A. Ventrice, R. S. Ruoff, *Carbon* **2009**, *47*, 145.

[31] N. Sharma, V. Sharma, Y. Jain, M. Kumari, R. Gupta, S. K. Sharma, K. Sachdev, *Macromolecular Symposia* **2017**, *376*.

[32] P. G. Ren, D. X. Yan, X. Ji, T. Chen, Z. M. Li, *Nanotechnology* **2011**, *22*, 055705.

[33] a) A. Siokou, F. Ravani, S. Karakalos, O. Frank, M. Kalbac, C. Galiotis, *Applied Surface Science* **2011**, *257*, 9785; b) L. Stobinski, B. Lesiak, A. Malolepszy, M. Mazurkiewicz, B. Mierzwa, J. Zemek, P. Jiricek, I. Bieloshapka, *Journal of Electron Spectroscopy and Related Phenomena* **2014**, *195*, 145.

[34] a) D. Lin, Y. Liu, Z. Liang, H. W. Lee, J. Sun, H. Wang, K. Yan, J. Xie, Y. Cui, *Nat Nanotechnol* **2016**, *11*, 626; b) H. Ye, S. Xin, Y. X. Yin, J. Y. Li, Y. G. Guo, L. J. Wan, *J Am Chem Soc* **2017**,

139, 5916; c) J. Rafiee, M. A. Rafiee, Z. Z. Yu, N. Koratkar, *Adv Mater* **2010**, *22*, 2151; d) R. Raccichini, A. Varzi, S. Passerini, B. Scrosati, *Nat Mater* **2015**, *14*, 271.

[35] a) R. Zhang, X. R. Chen, X. Chen, X. B. Cheng, X. Q. Zhang, C. Yan, Q. Zhang, *Angew Chem Int Ed Engl* **2017**, *56*, 7764; b) C. P. Yang, Y. X. Yin, S. F. Zhang, N. W. Li, Y. G. Guo, *Nat Commun* **2015**, *6*, 8058; c) Z. Liang, D. Lin, J. Zhao, Z. Lu, Y. Liu, C. Liu, Y. Lu, H. Wang, K. Yan, X. Tao, Y. Cui, *Proc Natl Acad Sci U S A* **2016**, *113*, 2862.

[36] a) Y. Kajikawa, S. Noda, *Applied Surface Science* **2005**, *245*, 281; b) T. Ito, T. Akiyama, K. Nakamura, *Journal of Crystal Growth* **2019**, *512*, 41; c) M. Ohring, *Materials Science of Thin Films*, Academic Press, San Diego, CA, USA 2001; d) M. Kumar, Govind, V. K. Paliwal, A. G. Vedeshwar, S. M. Shivaprasad, *Surface Science* **2006**, *600*, 2745.

[37] O. G. Bagmut, *Functional materials* **2019**, *26*, 6.

[38] a) D. Wang, W. Zhang, W. Zheng, X. Cui, T. Rojo, Q. Zhang, *Adv Sci (Weinh)* **2017**, *4*, 1600168; b) E. Bauer, H. Poppa, *Thin Solid Films* **1972**, *12*, 167.

[39] L. Guo, G. Oskam, A. Radisic, P. M. Hoffmann, P. C. Searson, *Journal of Physics D: Applied Physics* **2011**, *44*, 443001.

[40] a) N. Ikemiya, D. Iwai, K. Yamada, R. Vidu, S. Hara, *Surface Science* **1996**, *369*, 199; b) R. J. Nichols, D. Schröer, H. Meyer, *Electrochimica Acta* **1995**, *40*, 1479; c) E. B. Molodkina, M. R. Ehrenburg, P. Broekmann, A. V. Rudnev, *Electrochimica Acta* **2019**, *299*, 320.

[41] a) X. Zhang, R. Lv, A. Wang, W. Guo, X. Liu, J. Luo, *Angew Chem Int Ed Engl* **2018**, *57*, 15028; b) L. L. Lu, J. Ge, J. N. Yang, S. M. Chen, H. B. Yao, F. Zhou, S. H. Yu, *Nano Lett* **2016**, *16*, 4431; c) W. Luo, Y. Zhang, S. Xu, J. Dai, E. Hitz, Y. Li, C. Yang, C. Chen, B. Liu, L. Hu, *Nano Lett* **2017**, *17*, 3792.

[42] a) X. B. Cheng, T. Z. Hou, R. Zhang, H. J. Peng, C. Z. Zhao, J. Q. Huang, Q. Zhang, *Adv Mater* **2016**, *28*, 2888; b) T. Masese, K. Yoshii, M. Kato, K. Kubota, Z. D. Huang, H. Senoh, M. Shikano, *Chem Commun (Camb)* **2019**, *55*, 985.

[43] a) Z. Cao, B. Li, S. Yang, *Adv Mater* **2019**, 10.1002/adma.201901310, e1901310; b) Y. Gao, Z. Yan, J. L. Gray, X. He, D. Wang, T. Chen, Q. Huang, Y. C. Li, H. Wang, S. H. Kim, T. E. Mallouk, D. Wang, *Nat Mater* **2019**, 10.1038/s41563-019-0305-8.

[44] a) W. Liu, P. Li, W. Wang, D. Zhu, Y. Chen, S. Pen, E. Paek, D. Mitlin, *ACS Nano* **2018**, *12*, 12255; b) W. Liu, Y. Xia, W. Wang, Y. Wang, J. Jin, Y. Chen, E. Paek, D. Mitlin, *Advanced Energy Materials* **2018**, *9*, 1802918.

[45] a) L. Liu, Y. X. Yin, J. Y. Li, S. H. Wang, Y. G. Guo, L. J. Wan, *Adv Mater* **2018**, *30*, 1706216; b) S. H. Wang, Y. X. Yin, T. T. Zuo, W. Dong, J. Y. Li, J. L. Shi, C. H. Zhang, N. W. Li, C. J. Li, Y. G. Guo, *Adv Mater* **2017**, *29*, 1703729.

Table of Content

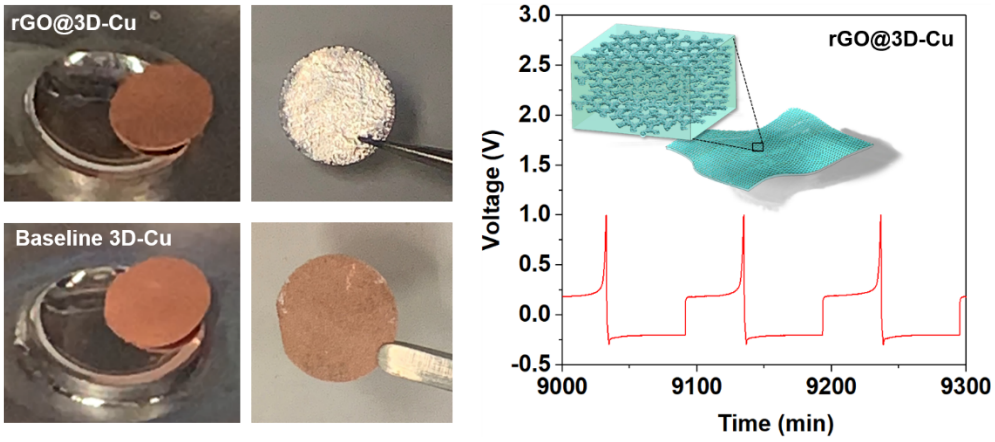

Three-dimensional copper current collector is functionalized with reduced graphene oxide to create a highly potassiophilic surface and allow stable K plating/stripping in a carbonate electrolyte. The reduced graphene oxide promotes layer-by-layer growth, while the three-dimensional collector geometry reduces the effective current and geometrically frustrates dendrites.